The anatomy of a star-forming galaxy II: FUV heating via dust

S. M. Benincasa [1,2]⋆ J. W. Wadsley,[2] H. M. P. Couchman,[2] A. R. Pettitt [3] B. W. Keller,[4] R. M. Woods[2]
and J. J. Grond[2]

[1] *Department of Physics, University of California, Davis, 1 Shields Ave., Davis, CA 95616, USA*
[2] *Department of Physics and Astronomy, McMaster University, L8S 4M1 Hamilton, Canada*
[3] *Department of Physics, Faculty of Science, Hokkaido University, Sapporo 060-0810, Japan*
[4] *Astronomisches Rechen-Institut, Zentrum für Astronomie der Universität Heidelberg, Mönchofstraße 12-14, D-69120 Heidelberg, Germany*

ABSTRACT
Far-ultraviolet (FUV) radiation greatly exceeds UV, supernovae (SNe), and winds in the energy budget of young star clusters but is poorly modelled in galaxy simulations. We present results of the first isolated galaxy disc simulations to include photoelectric heating of gas via dust grains from FUV radiation self-consistently, using a ray-tracing approach that calculates optical depths along the source–receiver sightline. This is the first science application of the TREVR radiative transfer algorithm. We find that FUV radiation alone cannot regulate star formation. However, FUV radiation produces warm neutral gas and is able to produce regulated galaxies with realistic scale heights. FUV is also a long-range feedback and is more important in the outer discs of galaxies. We also use the superbubble feedback model, which depends only on the SN energy per stellar mass, is more physically realistic than common, parameter-driven alternatives and thus better constrains SN feedback impacts. FUV and SNe together can regulate star formation without producing too much hot ionized medium and with less disruption to the interstellar medium compared to SNe alone.

Key words: radiative transfer – methods: numerical – ISM: structure – galaxies: ISM.

1 INTRODUCTION

Star formation is effectively regulated by how galaxies make the cold, dense clouds where stars form today. Far-ultraviolet (FUV) emission from massive stars heats the surrounding medium via the photoelectric effect (Watson 1972; Draine 1978; Wolfire et al. 1995). This FUV emission is often the dominant heating mechanism for the interstellar medium (ISM) and thus controls the warm versus cold phase balance. FUV is not absorbed by atomic hydrogen, giving it a long mean-free path (of order kpc) and it is thus far-reaching for dust surface densities characteristic of most nearby galaxies. Though FUV heating is strongest near young star clusters, it permeates the ISM and is non-local compared to other feedback such as UV radiation, winds, and supernovae (SNe). This work seeks to better understand the impact of both FUV and SNe on star formation and the ISM in a typical nearby galaxy.

In galaxy evolution, gas and star formation are intimately connected. The Kennicutt–Schmidt (KS) relation links the star formation rate (SFR) surface density with the total gas surface density, $\dot{\Sigma}_* \sim \Sigma_g^N$, where $N \sim 1.4$ (Schmidt 1959; Kennicutt 1998). The star-forming main sequence demonstrates a tight correlation between the galactic SFR and the total stellar mass of a galaxy (Brinchmann et al. 2004; Daddi et al. 2007; Noeske et al. 2007). These relationships have been established on local scales as well: on the kpc scale for the star-forming main sequence (e.g. Hsieh et al. 2017) and the sub-kpc scale for the KS relation (e.g. Bigiel et al. 2008). The original KS

relation probed typical surface densities $\Sigma_g \gtrsim 10 \, \mathrm{M_\odot \, pc^{-2}}$ (Kennicutt 1998). For $\Sigma_g \lesssim 10 \, \mathrm{M_\odot \, pc^{-2}}$, the KS relation steepens significantly (Kennicutt & Evans 2012, and references therein).

At high surface densities, $\Sigma_g \gtrsim 100 \, \mathrm{M_\odot \, pc^{-2}}$, combinations of SNe and radiation pressure are commonly invoked to regulate star formation (Ostriker & Shetty 2011; Shetty & Ostriker 2012). For surface densities between $10 \lesssim \Sigma_g \lesssim 100 \, \mathrm{M_\odot \, pc^{-2}}$, more representative of nearby galaxies, we expect SN feedback and stellar UV/FUV heating to play roles in regulating the SFR. At even lower surface densities, $\Sigma_g \lesssim 10 \, \mathrm{M_\odot \, pc^{-2}}$, star formation becomes much less effective. Here a key requirement for star formation may be the presence of two thermal phases in the ISM (Elmegreen & Parravano 1994). The absence of a persistent cold phase might sharply limit star formation in outer galactic discs (Schaye 2004).

At all surface densities, there is scatter from a single power law in the KS relation. In some regions, this scatter spans almost 2 dex in $\dot{\Sigma}_*$. This intrinsic scatter is not due to measurement error. In particular, single galaxies occupy tight regions in the $\dot{\Sigma}_* - \Sigma_g$ plane (e.g. Bigiel et al. 2008; Ostriker, McKee & Leroy 2010). This suggests that there are additional parameters affecting SFRs (e.g. Krumholz, Dekel & McKee 2012; Saintonge et al. 2017). One avenue to explain galaxy-to-galaxy differences in star formation at fixed surface density is through the strong connections between pressure, dense gas fractions, and star formation (e.g. Wong & Blitz 2002; Blitz & Rosolowsky 2004; Herrera-Camus et al. 2017; Gallagher et al. 2018). Galactic mid-plane pressure, in particular, can be linked to SFRs (Ostriker et al. 2010; Blitz & Rosolowsky 2006).

In normal spiral galaxies, old stars dominate the vertical gravity within discs. Thus pressure-based analysis strongly links SFRs to

⋆ E-mail: benincasa.9@osu.edu

the total stellar mass and naturally explains why stars are likely to continue forming where stars have formed previously. This motivates star formation laws of the form $\dot{\Sigma}_* \propto \Sigma_*^a \Sigma_g$ with $a \sim 0.5$ as in Blitz & Rosolowsky (2006). Shi et al. (2018) find that a fit such as $\dot{\Sigma}_* \propto (\Sigma_*^a \Sigma_g)^b$, where $a = 0.5$ and $b = 1.09$ has significantly less scatter than a traditional KS relation for their observed data set.

Ostriker et al. (2010) attributed the bulk of star formation regulation to FUV, but did not independently treat turbulent support even though they recognized that it may be more important (see also: Herrera-Camus et al. 2017). Simulations have also shown that ISMs are not well characterized as just two simple, distinct phases (Kim & Ostriker 2015; Benincasa et al. 2016). These factors motivate revisiting the role of FUV with more comprehensive treatments.

1.1 Using simulations to study galactic star formation

Isolated galaxy simulations are an ideal place to study the structure of the ISM and star formation; they offer both high resolution and the full galactic context without complicating factors. There is a strong body of work studying the ISM using isolated galaxy simulations. Most studies focus on the formation and evolution of GMCs, as the intermediate step between diffuse gas and star formation (e.g. Tasker & Tan 2009; Benincasa et al. 2013; Pan et al. 2015; Rey-Raposo et al. 2017; Duarte-Cabral & Dobbs 2017; Dobbs et al. 2018; Pettitt et al. 2018). Other studies focus on the stability of gas, and searching for signatures of star formation (e.g. Nguyen et al. 2018; Agertz, Romeo & Grisdale 2015; Grisdale et al. 2018; Benincasa et al. 2016).

Stellar feedback has historically been the main approach for regulating star formation in galaxy simulations. Such feedback can be tuned to limit the amount of star-forming gas until SFRs are acceptable. A second, even simpler approach is to directly limit the efficiency of star formation, as was done in the AGORA isolated galaxy code comparisons (Kim et al. 2016). When free parameter choices are exploited in this way, simply regulating star formation is not a meaningful result. Simulations also have effective parameter freedom such as restrictions on the gas equation of state and resolution limits on gravity that effectively hold up the ISM. These points argue for high-resolution simulations with parameter-free, first-principles models as much as possible. However, key processes such as star formation and early feedback phases are essentially impossible to resolve in galaxy simulations so some freedom in the models is unavoidable.

Current SN feedback implementations often dramatically blow away gas from the simulated ISM. This partly reflects the need to regulate the baryon content of entire galaxies so as to meet abundance matching constraints (Keller, Wadsley & Couchman 2016). While this may effectively regulate star formation in the galaxy as a whole, it hampers our ability to study the ISM–star formation connection in galaxy simulations.

1.2 The role of FUV heating

FUV radiation is the dominant heating process for warm and cold neutral gas in the ISM. It does this by ejecting electrons from dust grains which deposit their energy in the gas. In the energy budget of a typical stellar cluster, FUV radiation provides nearly two orders of magnitude more energy than SNe or stellar winds (Starburst99, Leitherer et al. 1999). Ionizing UV heating is powerful but it is absorbed locally within star-forming clouds which must be resolved before it plays a major role. In contrast, because FUV is not absorbed by atomic hydrogen, it has a long mean-free path, making it far-reaching compared to other types of feedback.

As noted above, Ostriker et al. (2010) analytically explored FUV heating to regulate star formation. The model did not include a distinct treatment of SNe or feedback other than FUV. Instead, it assumed turbulent pressure was proportional to thermal pressure which in turn was controlled by FUV. Tying turbulence to FUV this way obscures the role for FUV as a regulator. Remarkably, given its potential importance, there has been little other analytical work on star formation regulation taking FUV into account.

Different forms of support, such as warm gas due to FUV, hot gas due to SNe and turbulence behave differently within the ISM. Whereas gas that has been heated by SNe can leave the disc in an outflow, FUV heated gas remains in the ISM. The role FUV plays in regulating star formation cannot be disentangled from its role in maintaining the structure of the ISM. The necessity of producing a realistic ISM is a powerful constraint that should help us understand the roles of different feedback.

Combining both SNe feedback and FUV heating provides simulations with a new dimension to explore. However, FUV heating is not commonly employed as a feedback. If radiative transfer is not available, FUV radiation can be included as a prescribed background heating rate (e.g. Kim, Kim & Ostriker 2011; Benincasa et al. 2016; Hu et al. 2017) but this is not self-consistent. It does not focus heating where stars are being formed both spatially and temporally. For very small volumes, a uniform FUV field can be tied to the SFR as in Kim et al. (2011).

Numerical works have begun to include radiation fields derived from the stellar sources for entire galaxy simulations. Forbes et al. (2016) studied the effect of photoelectric heating on dwarf galaxies under the assumption that they were entirely optically thin to FUV due to their low metallicity. They conclude that FUV is a very effective stellar feedback in these small galaxies ($\lesssim 0.01$ the Milky Way in total mass).

Typical galaxies like the Milky Way are optically thick to all UV radiation. The mean-free path for FUV in the ISM is ~ 1 kpc which means sources up to ~ 10 kpc away may contribute to the local flux (see Appendix A). One approach is to model this with local absorption estimators. Hopkins, Quataert & Murray (2012) and related papers (e.g. Oñorbe et al. 2015) employ a Sobolev-like approximations, where gas column is estimated as $\Sigma \sim \rho L$ with a characteristic length $L = \rho/|\nabla\rho|$. This approximation was designed for radiation escape or self-shielding estimates at the receiving gas (e.g. Gnedin, Tassis & Kravtsov 2009). Instead, these simulations assume an optical depth associated with the easiest escape path at the source, assumed to be $-\nabla\rho$. Starlight experiences a fixed attenuation regardless of whether it travels in this direction or not. Similarly, setting L equal to the Jeans length (Lagos et al. 2015; Marinacci et al. 2017; Diemer et al. 2018) assumes the local gas is smooth, bound, and the only source of absorption. It also prevents directional variations.

Even simple galactic radiative transfer models require directional dependence (e.g. Byun, Freeman & Kylafis 1994). Wang et al. (2018) show that UV extinction varies by a factor of ~ 4 depending on inclination for galaxies at intermediate redshifts. Local absorption approximations are unlikely to be accurate except for photons leaving vertically (e.g. face-on mock images). To study photoelectric heating, we must follow FUV radiation moving laterally within the galaxy, where gas typically sees photons that have traversed several kpc of ISM structure. Self-consistent FUV heating via full radiative transfer is the best way to simultaneously quantify its roles in regulating star formation and setting the structure of the ISM.

A promising approach to full radiative transfer is the M1-closure (Aubert & Teyssier 2008) which uses an explicit flux variable

to improve the directionality and diffusiveness of prior moment methods such as flux-limited diffusion. M1 still merges crossing rays and cannot quite match detailed ray tracing such as variable Eddington tensor (VET, Davis et al. 2014), but should be reasonable for average intensities required for heating. A common associated choice is a dramatically reduced speed of light to allow larger time steps. M1 has been added to several major codes (Rosdahl et al. 2013; Kannan et al. 2019; Hopkins et al. 2020). Rosdahl et al. (2015) ran a high-resolution galaxy with multiband radiative transfer but did not include a FUV band. Hopkins et al. (2020) have recently run M1-radiative transfer on galaxies including an FUV band. Their basic results do not show FUV to be an important regulator. However, they have not yet presented detailed results on FUV. Their results also assume relatively high opacities, so may be taken as a lower limit on the possible effect of FUV.

In the current work, we use the TREVR (Grond et al. 2019) radiative transfer algorithm to implement self-consistent FUV heating in simulations of entire galactic discs. This is a ray-tracing approach and thus distinct from moment-based approaches like M1 and thus complementary to existing work.

In Paper I (Benincasa et al. 2016), we explored the coupling between the ISM, its pressure, star formation, and feedback. The high-resolution, isolated galaxy models employed there used specified FUV fields, a parameter-driven SN model and a fixed galactic potential without an old stellar disc. Paper I demonstrated that time-averaged pressure balance is a key feature of well-resolved, simulated galaxies. It also established strong connections between properties such as scale height, gas surface density, and SFRs. In that work, SNe were the primary source of pressure support and FUV was not self-consistently treated. The isolated galaxy of Paper I also did not have an old stellar disc which prevented direct comparisons to similar nearby galaxies. The current work corrects these oversights.

In this paper, we explore the impact of self-consistent FUV heating from radiative transfer in combination with physically well-constrained SN feedback on the ISM and star formation in an isolated galaxy with a live halo and old stellar disc. The remainder of this paper is laid out as follows: in Section 2, we describe our chosen galaxy model, a modification of the isolated disc test cases used in the AGORA comparison project. In Section 3, we describe the model for radiative transfer that we employ in this work. We then contrast different combinations of feedback choices and their roles in setting different galaxy and ISM properties in Sections 4 and 5.

2 GALAXY MODEL

Our isolated galaxy model is a higher-resolution version of the initial conditions from the AGORA High-resolution Galaxy Simulations Comparison Project (Kim et al. 2014, 2016). The galaxy has a live stellar disc and bulge, as well as a live dark matter halo. The dark matter halo has an NFW density profile (Navarro, Frenk & White 1997). The halo has $M_{200} = 1.074 \times 10^{12}$ M$_\odot$ and a halo concentration parameter, $c = 10$. The stellar disc has an exponential density profile with a total mass of 3.438×10^{10} M$_\odot$. The stellar bulge has a total mass of 4.927×10^9 M$_\odot$ and follows a Hernquist (1990) profile.

We began with the standard (low) AGORA resolution initial condition, but then split each particle 64 times to increase the resolution. The dark matter halo has 6.4 million particles, each of mass 1.956×10^5 M$_\odot$. The stellar disc and bulge combined have 7.2 million particles, each of mass 5360 M$_\odot$. The gas disc is composed of 6.4 million particles, each of mass 1342 M$_\odot$. We employ the standard GASOLINE piecewise polynomial gravitational softening,
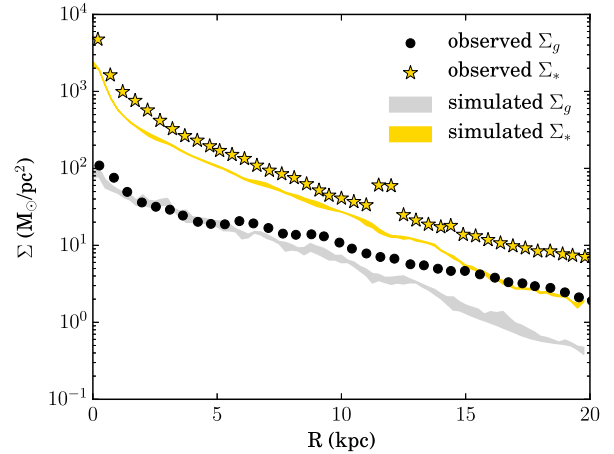

Figure 1. A comparison of our simulated galaxy surface density to the gas surface density of the sunflower galaxy, NGC 5055. The grey bar shows the range of simulated Σ_g and the yellow bar the range of simulated Σ_*, measured after 200 Myr of evolution. The filled circles show the total gas surface density, Σ_{HI+H_2} as reported in Bigiel et al. (2008). The filled stars show the total stellar surface density as reported in Leroy et al. (2008). Our galaxies show good agreement with NGC 5055, within 30 per cent, until the outer regions of the disc ($R \gtrsim 10$ kpc).

with a softening length of 80 pc (so that force is Newtonian at a distance of 160 pc).

We picked the public AGORA galaxy IC to facilitate comparisons with other work, including the original study (Kim et al. 2016) and newer work that also uses it (e.g. Agertz et al. 2015; Grisdale et al. 2017, 2018; Semenov, Kravtsov & Gnedin 2017, 2018). However, we note that this galaxy has a significantly higher surface density than typically estimated for the Milky Way, its ostensible target (e.g. Nakanishi & Sofue 2016). It is still in the typical range for normal spiral galaxies. In fact, the AGORA IC has similar characteristics with NGC 5055, the sunflower galaxy.

In Fig. 1, we plot a comparison of the gas and stellar surface density in our simulations to those of NGC 5055. The total gas surface density is a combination of THINGS H I (Walter et al. 2008) and H$_2$ as measured by HERACLES CO (Leroy et al. 2009). The stellar surface density is from the *GALEX* nearby galaxy survey as reported in Leroy et al. (2008). Both of the model profiles are similar to the observational data within 10 kpc. The observed stellar surface density is $\sim$ 30 per cent higher than in our galaxy. These radial distributions, especially the stellar distribution, are potentially important quantities in determining the outcomes of galaxy scaling relations (Ostriker et al. 2010).

For comparison, Paper I (Benincasa et al. 2016), used a static potential with no old stellar population. The presence of the heavy, old stellar disc has the effect of stabilizing the gaseous disc, but also acts as a driver for spiral structure. Locally, the old stellar disc is an important source of vertical gravity to limit the gas scale height.

3 METHODS

We simulated a suite of different feedback treatments, as listed in Table 1, on our galaxy model to study star formation and ISM evolution over a period of 400 Myr. This allows time for the galaxy to settle into a well-regulated state if one exists. These feedback treatments and other aspects of the simulations are described in this section.

Table 1. List of simulation details.

Name	SNe	FUV	Cosmic rays	$E_{\rm SN}$ (erg)
FB50	✓	✗	✓	5×10^{50}
FUVFB50	✓	✓	✓	5×10^{50}
FB10	✓	✗	✓	10^{50}
FUVFB10	✓	✓	✓	10^{50}
FUV*	✗	✓	✓	None

We use the modern SPH (smoothed particle hydrodynamics) code GASOLINE (Wadsley, Stadel & Quinn 2004; Wadsley, Keller & Quinn 2017). As demonstrated in Wadsley et al. (2017), modern SPH, as implemented in GASOLINE, performs particularly well for supersonic, turbulent gas such as that present in disc galaxies. The simulations employ star formation, feedback, and metal cooling following the standard prescriptions presented in MUGS2 (Keller, Wadsley & Couchman 2015). These models have been successful in producing realistic disc galaxies, including stellar content over cosmic time, in cosmological zoom-in simulations (Keller et al. 2016). A new component in this work is the inclusion of radiative transfer to implement self-consistent FUV radiation from young stars throughout the entire disc.

3.1 Radiative transfer

Outside hot superbubbles, the ISM is primarily heated by the photoelectric effect on dust grains due to FUV radiation (Wolfire et al. 2003). X-rays and cosmic rays are of secondary importance except at very low densities or in dense, shielded gas. Gas-ionizing UV radiation is of comparable importance in principle, except that the high optical depths limit it to H II regions occupying a fraction of a percent of the ISM. Thus when studying the typical ISM (0.01–$100 \, {\rm cm}^{-3}$, 100–10000 K), FUV is the most important heating process and it sets the temperature.

In this study, we fully propagate the FUV flux emitted by young star clusters estimated using integrated spectra from STARBURST99 over the band 912–1550 Å (Leitherer et al. 1999). This is the first time this has been done on-the-fly using ray tracing with absorption in a full, isolated galaxy disc simulation. The radiation field is modelled as a single FUV band as discussed in Grond et al. (2019). This band heats the gas via the photoelectric effect on dust which is assumed to be linear in the local gas metallicity with a 3 per cent heating efficiency (a fairly typical value, Tielens 2005). We employ an opacity due to dust absorption of $300 \, {\rm cm}^2 \, {\rm g}^{-1}$ (scaled linearly from solar metallicity). We note that the Lyman–Werner band, which dissociates molecular hydrogen, is also in the FUV range. However, the current work does not treat molecular gas formation or destruction.

The simulations presented here employed the original version (Woods 2015) of the radiative transfer algorithm, TREVR, detailed in Grond et al. (2019). TREVR (Tree-based REVerse Raytracing) is a novel algorithm for computing radiation fields. TREVR estimates local, angle-averaged intensities for heating and chemistry based on reverse ray tracing back to available sources (which are merged using the tree) and includes absorption by intervening gas and dust (but not scattering in current versions). The original TREVR algorithm did not use adaptive accuracy controls. It slowed the code by roughly a factor of 2 when self-consistent FUV was being computed. The final version of TREVR (Grond et al. (2019), not used in the calculations presented here), includes detailed error control via refinement at the expense of considerable extra computation. As such, it would not

be feasible (at present) to use for full simulations but is useful for generating highly accurate radiative transfer results for comparison at a specific output time. In Appendix A, we use it to show that the fast, original scheme is accurate for FUV, particularly when it comes to ISM temperatures.

This work recreates a typical Milky Way-like ISM similar to that of Wolfire et al. (2003), who modelled heating rates and ISM phases as a function of galactic radius. For fixed opacity, clumping in radiative transfer tends to reduce the absorption relative to a uniform medium, as most rays miss denser structures. Wolfire's FUV model employed a relatively low opacity value ($\sim$300 cm^2 g^{-1} without scattering) to be used with smoothed, average ISM densities (e.g. without molecular clouds or smaller-scale structures). The current work has intermediate resolution, with limited ability to model denser gas $\gtrsim$100 cm^{-3} and thus clouds-scale clumping effects on radiative transfer are not present. Given these considerations, we argue that 300 cm^2 g^{-1} is a low but reasonable opacity. Thus, this work could be considered an upper bound on the effect of FUV.

For other radiation fields and heating processes (including EUV and cosmic rays), we used fixed background rates as in Paper I (Benincasa et al. 2016). Together with the density and temperature, these determine the local, non-equilibrium ionization state of the gas. We note that photoionization and photodissociation due to local radiation sources directly impacts a tiny portion of the ISM, on parsec scales. At the current resolution, we do not capture such dense star-forming subclumps ($\gtrsim$10^4 cm^{-3}). Our star-forming clouds (100–1000 cm^{-3}) are readily destroyed by the stellar feedback processes described below.

3.2 Feedback

We employ the superbubble feedback method as detailed in Keller et al. (2014). This model includes the effect of electron conduction to model the combined mechanical output of young clustered stars. A self-similar solution was first presented by Weaver et al. (1977). Superbubbles form when fast outflows from massive stars (such as SNe) shock and merge into an expanding hot bubble. The bubble pressure sweeps up a cold shell of ISM. Electron conduction regulates the interior mass and temperature ($\sim$3 × 10^6 K) of the bubble. The steep power-law dependence of conduction on temperature makes the model insensitive to the conduction coefficient (e.g. effects due to tangled magnetic fields) so there are effectively no free parameters. The bubble's behaviour is strongly determined by how much energy is injected and the density of the medium, which are easily determined in simulations. The model includes conduction, evaporation of cool into hot gas, and a subgrid phase representing the swept up cold gas shell. The subgrid phase is short-lived as evaporation rapidly generates well-resolved hot bubbles. Both phases cool normally. These properties make the outcomes insensitive to resolution (Keller et al. 2014).

Commonly employed prior methods, such as that used in Benincasa et al. (2016), have several free parameters (e.g. a parameter for an energy transfer time-scale or a cooling time and a parameter to determine how much mass is affected). Together with resolution, these affect basic outcomes such as feedback temperatures. This reflects the fact that the structure of the ISM has typically been a secondary concern as long as the overall SFR was acceptable. Prior work showed that the strong SNe feedback was highly destructive to the ISM in a manner that suggested too much of the kinetic energy was being deposited there. One long-standing approach is to hydrodynamically decouple feedback material from the ISM in galaxy simulations (e.g. Springel & Hernquist 2003).

We would like to tightly constrain the role of each feedback. However, for SNe in particular, there is uncertainty regarding how much energy directly affects the ISM (Gentry, Madau & Krumholz 2020). Recently, El-Badry et al. (2019) explored superbubbles with high-resolution, 1D simulations and found that additional energy could be lost during evaporation. In addition, Keller et al. (2016), found that 50 per cent of the SNe energy going into the superbubbles was sufficient to correctly simulate the baryon content of Milky Way-like galaxies and their progenitors over cosmic time. We take this as an energy upper limit. However, as noted above, strong coupling to the ISM by SNe outflows is an unavoidable consequence of limited resolution. An equivalent statement of this issue is that the effective Reynold's number of simulations is generally much lower than that of the real ISM so that boundary layers and viscous coupling are overestimated. A crude way to model this is to assume some part of the feedback energy vents directly to the galactic halo, as in Springel & Hernquist (2003), and that such losses do not immediately affect the ISM.

For these reasons, we use two different SNe feedback strengths, 50 per cent and 10 per cent of the maximum value, or 5×10^{50} and 10^{50} erg, respectively, to attempt to bracket the range of possibilities.

3.3 Star formation

We use a common star formation prescription, where stars form following a Schmidt law:

$$\frac{\mathrm{d}\rho_*}{\mathrm{d}t} = c_* \frac{\rho_g}{t_{\mathrm{dyn}}}, \tag{1}$$

where ρ_* is the density of new stars formed, ρ_g is the density of eligible gas, $t_{\mathrm{dyn}} = 1/\sqrt{4\pi G \rho_g}$ is the dynamical time, and c_* is the chosen efficiency. Gas is considered eligible for star formation if it lies above a set density threshold, lies below a maximum temperature and belongs to a converging flow. This is a typical star formation method (e.g. Katz 1992). The small fraction of particles that are currently in a two-phase state cannot form stars. We assume that these particles, near recent star formation events, are analogous to unbound GMCs. In this study, we employ a c_* of 0.05, a density threshold of 100 cm^{-3}, and a maximum temperature threshold of 1000 K.

4 RESULTS

4.1 Global galaxy properties

We begin by considering the basic properties of the galaxies in our suite after 400 Myr of evolution (detailed in Table 1). As a first diagnostic, we consider the visual appearance of the galaxies. Fig. 2 shows face-on images for different quantities of interest. The leftmost panel shows the total gas surface density of the disc. The second panel shows the gas surface density of the disc when considering only gas above 100 cm^{-3}, the analogue of molecular gas in our simulations. The third panel shows a synthetic stellar map for young stars. To show the primary sources of FUV, we show only stars that have formed in the last 100 Myr (Salim et al. 2007; Murphy et al. 2011; Kennicutt & Evans 2012). Finally, we show a synthetic stellar map for all stars, to show how the stellar disc has built up over time in each case: this includes only stars that have formed since the start of the simulation and excludes the initial stellar disc.

If we consider each of the gas panels in Fig. 2, the cases that have both superbubble and FUV feedback are qualitatively similar:

in each case, we see a flocculent spiral with gas that extends far beyond the extent of the star-forming region of the galaxy. The cases with a lower SNe feedback energy, FUVFB10 and FB10, have more apparent spiral structure than those with higher feedback energy. This manifests itself in the stellar disc as narrower spiral arms. There is, however, a stark contrast when we consider the case with only FUV heating and no other form of feedback. In the gas we can see that there is a high degree of fragmentation for this galaxy. This results in highly clustered star formation and a dense stellar nugget at the galaxy's core, as well as overconsumption of gas in the galactic disc.

The global SFR for each of the galaxies is plotted on the left-hand side of Fig. 3. The SFR provides us with concrete evidence of what is suggested in the maps in Fig. 2. First, FUV heating alone cannot regulate star formation in the galaxy. When FUV heating is the only source of feedback, the SFR is very high and only begins to decrease as the galaxy runs out of gas (black line). This is similar to no feedback cases in this and the mode of excessive star formation via large gas clumps.

Simulations with SN feedback stabilize their SFR by ∼200 Myr. The cases with superbubble feedback only are plotted as purple lines, while cases with FUV heating and superbubble are plotted in green. As expected, decreasing the feedback energy results in more star formation (see Paper I: Benincasa et al. 2016). Further, adding FUV heating on top of superbubble feedback results in a small decrease in the SFR, of order 30 per cent.

Another notable feature in these SFRs is how quickly the SFR settles or dips after the initial burst. The cases with both modes of feedback (green lines) are able to regulate and end the burst more quickly than the cases with only superbubble feedback (purple lines). This timing difference is approximately 10 Myr. In our chosen feedback model, SNe do not begin until 4 Myr after a star is born. FUV radiation however, begins heating the surrounding environment immediately after the star is born. This means that regulation can begin more quickly.

Next, we compare the gas scale heights for each of the galaxies, shown on the right-hand side of Fig. 3. In this figure, we plot both the total gas scale height (left) and the H I gas scale height (right). For comparison, we also plot the H I scale height for NGC 5055 as quoted in Patra (2019). We find that the galaxies with the most SN feedback energy have the highest scale heights. The response is somewhat sublinear, as shown in Paper I due to the dependence of gravity on height in discs.

The SN energy injection rate is proportional to the SFR multiplied by 5 for the FB50/FUVFB50 cases, 1 (unchanged) for the FB10/FUVFB10 cases and zero for the FUV-only case. The inclusion of FUV heating leads to a decrease in the scale height because the warm medium it generates provides pressure support (discussed more in Section 5). This allows for a decreased role for superbubble feedback in supporting the gas and the lower SFR. Superbubble feedback energy is responsible for inflating the disc and causing outflows from the ISM.

4.2 Pressure balance in the ISM

Pressure facilitates the regulation of star formation in galaxies and it is connected to the dense gas fraction (Blitz & Rosolowsky 2004, 2006; Ostriker et al. 2010). We explore the pressure balance in our simulated galaxy discs in this section, following the approach of Paper I.

The SFR in a galaxy is set by the balance between the pressure required and the pressure support. The level of pressure required is
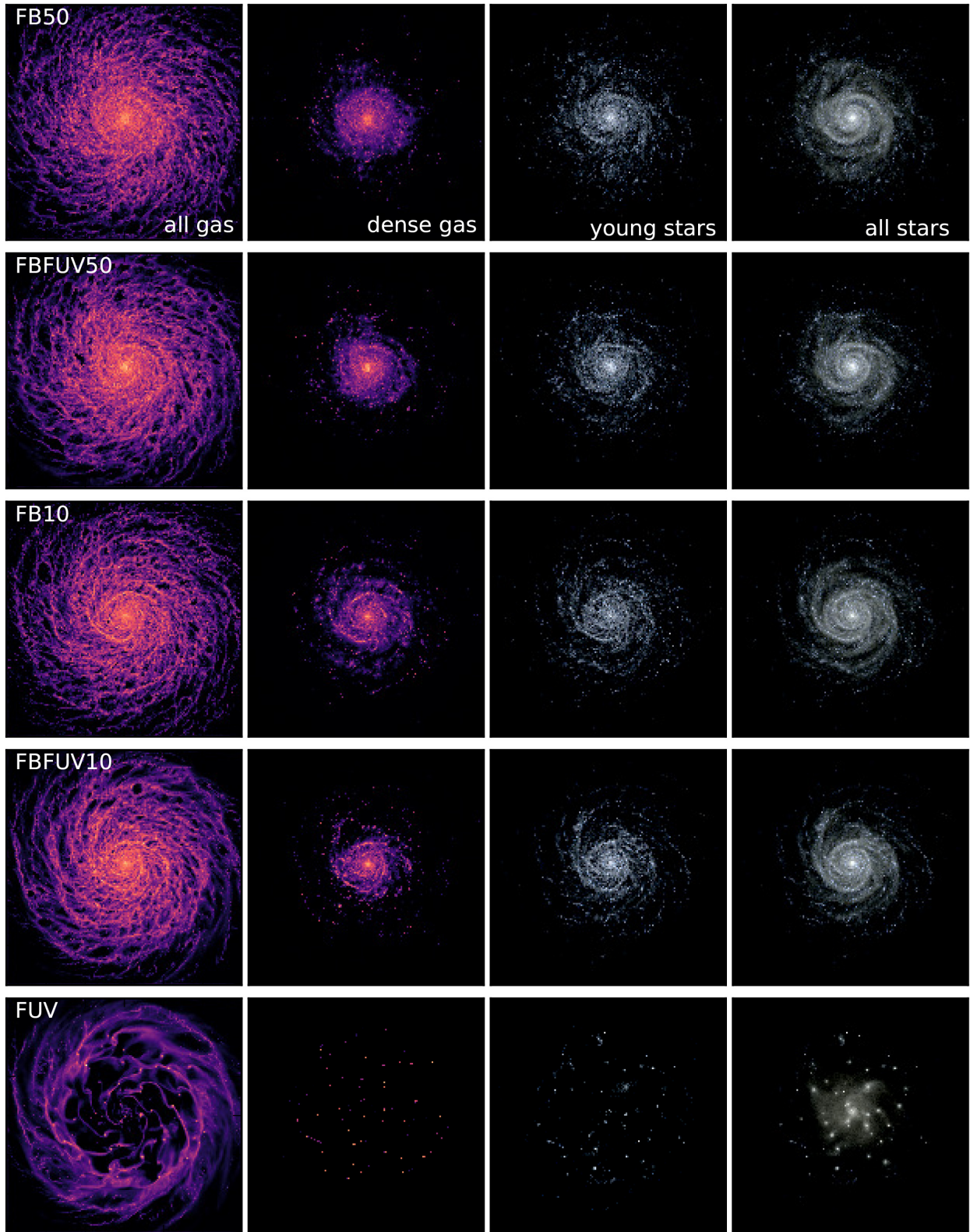
Figure 2. Gas and stellar maps for the galaxies in the simulation suite. Left: total gas surface density. Middle left: dense gas surface density, which here means any gas with $n > 100$ cm^{-3}. In the gas surface density columns, the colour-scale runs from 1 (black) to 500 M$_\odot$ pc^{-2}. Middle right: young stellar luminosity; here young stars have formed less than 100 Myr in the past. Right: stellar luminosity for all stars formed since the start of the simulation. When both superbubble feedback and radiative transfer are included there is very little difference in these maps from galaxy to galaxy. However, it is clear to order that FUV heating alone cannot regulate star formation and sustain galactic disc, as seen in the final row.
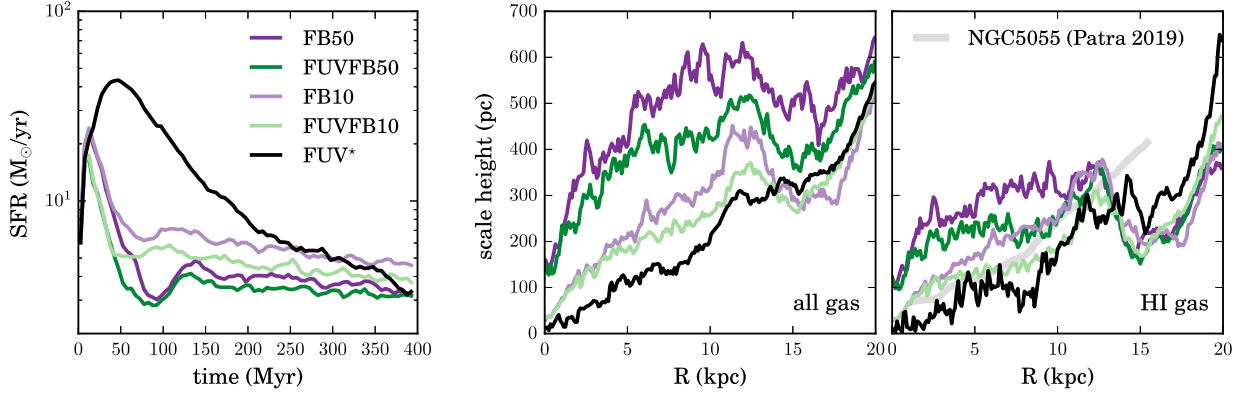
Figure 3. A comparison of the global SFR and the gas scale heights for the galaxies in the suite. Left: the global SFR. In all of the galaxies that include both superbubble feedback and FUV heating, there are only small changes in the SFR. However, when the only form of feedback is FUV heating, there is a dramatic increase in the amount of star formation. This galaxy can only decrease its SFR by consuming a significant amount of the star-forming fuel. Middle: the scale height for all gas in the galaxies. In this case, the difference between including only FUV heating and both modes of feedback is less stark in contrast. As expected, cases with stronger superbubble energy have larger scale heights. Interestingly, including the radiative transfer on top of superbubble leads to a decrease in the scale height. Right: the scale height for H I gas, the distribution as quoted in Patra (2019) is plotted in grey for comparison. The case with FUV heating and a lowered feedback efficiency, FUVFB10, shows the best agreement while still regulating star formation. The scale height shown here is measured at 400 Myr.

set by gravity in the disc:

$$P_R = P_{dm} + P_g + P_*$$

$$= \frac{1}{2}\Omega^2\Sigma_g H_g + \frac{1}{2}\pi G \Sigma_g^2 + \pi G \Sigma_g \Sigma_* \left(\frac{H_g}{H_g + H_*} \right) \quad (2)$$

where Ω is the rotation rate, Σ_g is the gas surface density, H_g is the gas scale height, Σ_* is the stellar surface density, and H_* is the stellar scale height. The dark matter halo primarily sets the rotation rate and the vertical component is proportional to Ω^2. See Benincasa et al. (2016) for a detailed derivations of these terms. This required pressure, P_R, is the pressure needed to support the weight of the ISM in a state of hydrostatic equilibrium.

The pressure support we measure in the disc is calculated by:

$$P_S = P_{th} + P_{hot} + P_{turb}$$

$$= \frac{\Sigma_g}{2 H_g} \left(\frac{2}{3}u_{th} + \frac{2}{3}u_{fb} + v_z^2 \right)_{z=0}. \quad (3)$$

This is the mid-plane support and so all these quantities take on their mid-plane values. The mid-plane density, $\rho_{g,0}$, is well approximated by the gas surface density divided by twice the gas scale height, H_g. P_{th} refers to warm gas primarily heated by FUV radiation, whereas P_{hot} refers to SNe heated gas in the mid-plane. In Paper I, only the hot component was directly linked to star formation. In the current simulations, FUV is linked not only to local star formation but young stars within several kpc via radiative transfer.

In Fig. 4, we plot a selection of pressure quantities of interest. To discern the relative importance of each, we plot these as ratios with the total pressure in the top row We note that while here we plot a comparison of the FB10 cases, the trends discuss hold also for the higher feedback, FB50, cases as well. The top left of Fig. 4 shows the amount of support from P_{hot}, the top middle shows the amount from P_{th} and the top right shows the amount from P_{turb}. For clarity, on the two of the galaxies in the suite are plotted, FUVFB10 (green) and FB10 (purple). As expected, adding the FUV heating decreases the role for superbubble feedback in supporting equilibrium (P_{hot}). There is very little impact on the turbulent pressure support in the disc.

In the bottom row of Fig. 4, we plot the total pressure, as well as the state of pressure equilibrium in two sample discs. In the bottom left panel, the total pressure support for FUVFB10 and FB10 are plotted. The total pressure is equal, so we can see that changing the types of feedback merely changes the partitioning of the pressure into different forms of support.

The role of FUV radiation is to heat cold neutral gas. When FUV radiation is included, as in case FUVFB10, a larger fraction of the pressure support is held as a thermal component (top middle panel of Fig. 4). In order for the total galactic pressure to remain the same, this must be made up by super bubble energy, or P_{hot}. This manifests itself as changes in the phase structure of the ISM, as will be shown in Section 5. This demonstrates that FUV is critical to support the ISM in the outer parts of galaxies.

The final two plots show the state of pressure equilibrium in FUVFB10 and FUV*. What is plotted here is different from what is plotted in Benincasa et al. (2016) in the sense that we do not have to rely on time averaging to see the differences. In these simulations, we have an old stellar disc whose gravity dominates the required pressure component. In Paper I, gas determined the dynamics of the galaxy, which made it hard to link the simulations to nearby galaxies.

This picture is different when we consider the case with FUV heating and no superbubble feedback, FUV*. This is the only case where we do not see global pressure equilibrium. The imbalance is already in place after 50 Myr. FUV heating by itself is unable to regulate the SFR. This results in the fragmentation of the gas into dense knots and a very high level of gas consumption. This significantly alters the distribution of gas throughout the disc. FUV heating due to star formation is more intense in the knots but is not effective as a feedback because it cannot unbind them. However, the scale height for this galaxy, shown in Fig. 3 is smaller than all of the other galaxies: less than 100 pc in the inner regions of the disc. At this scale height, we are approaching the resolution limit set by the gravitational softening. Thus, this pressure disagreement requires further investigation at higher resolution. We note that in GASOLINE, hydrodynamic resolution is not limited so it favours support over collapse below the gravity resolution scale.
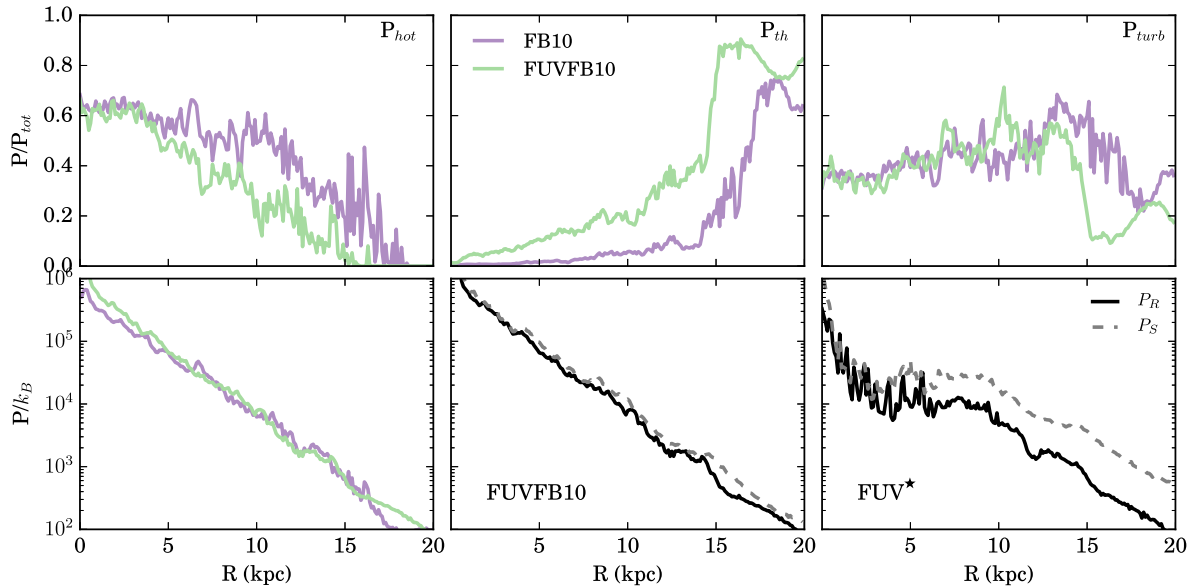
Figure 4. Comparison of the division of pressure in different means of support. Left: contribution in each galaxy to P_{hot}. Middle: contribution in each galaxy to P_{th}. Right: contribution in each galaxy to P_{turb}. Adding FUV heating does not change the amount of pressure held in the turbulent component. However, it does lead to more support coming from a thermal component in the ISM. We have plotted only our lower feedback galaxies for clarity, but these trends hold for the FB50 cases as well.
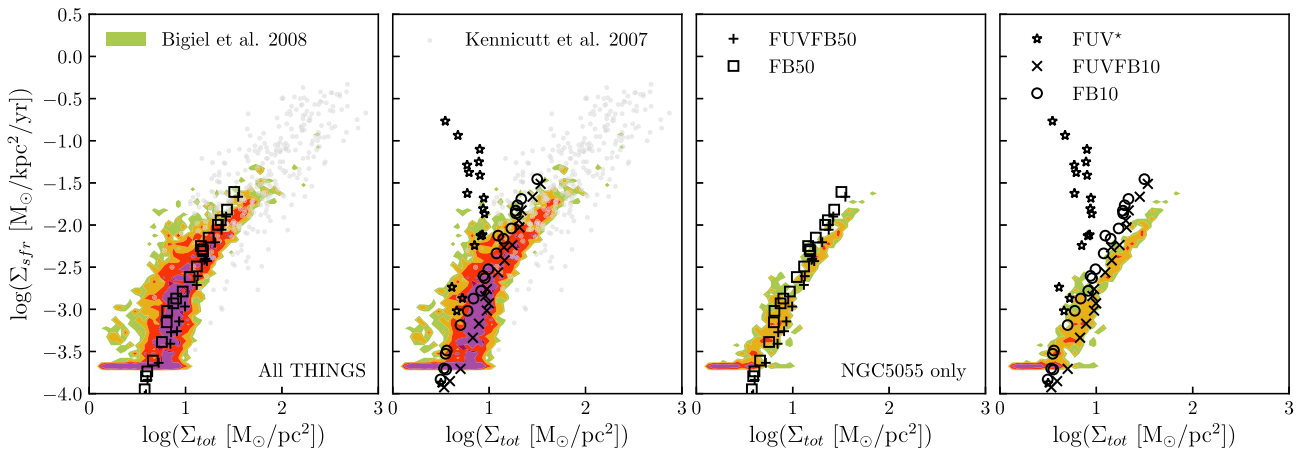

Figure 5. The KS relation for our simulated galaxies compared to observational samples. The black symbols show the five galaxies in our suite. For our data, we plot only values for radii outside 2.5 kpc. In the leftmost two plots, the coloured contours show the space occupied by local measurements for all the THINGS sample; and in the rightmost two plots, the contours show the space occupied by NGC 5055 (Bigiel et al. 2008). The dots in the top row show the local measurements in M51 from Kennicutt et al. (2007).

4.3 The distribution of star formation

The KS relation is an empirical relation used to characterize the star-forming ISM in galaxies. It is important to note that the spread in this relation is real, as explored by Leroy et al. (2008) and others. It cannot be accurately characterized with a single power law and depends on individual galaxy properties beyond the local gas surface density. Thus when we say KS relation, we are referring to the specific relationship between SFRs and gas surface densities for an individual galaxy and not a specific power-law fit. In Fig. 5, we plot the KS relation for the simulated galaxies and compare to a selection of observational data. The contours in Fig. 5 show locally measured data from two different surveys. The coloured contour shows the space occupied by the THINGS galaxies as reported in Bigiel et al. (2008); these measurements are taken at 750 pc scales.

The small grey circles show local measurements of M51 as reported in Kennicutt et al. (2007); these measurements are taken on 300 pc scales. In the left two plots, we compare to the entire sample of galaxies, whereas in the right two plots, we compare specifically to NGC 5055. The simulated galaxies are plotted as the different open symbols. These measurements were taken in 500 pc radial annuli, to agree with the resolution of the radial measurements reported in Leroy et al. (2008). For the SFR surface density, we consider only the stars that have formed in the last 100 Myr. Additionally, we take only measurements outside a galactic radius of 2.5 kpc.

Generally, our simulated data agree with the observational trend for cases with SN feedback. The relation for the FUV⋆ case further shows that FUV heating along cannot regulate the SFR. There the relation between Σ_g and Σ_{sfr} is nearly vertical, such that pieces of the galaxy at the same Σ_g can have SFRs that vary by several orders of

magnitude. This is in contrast to Ostriker et al. (2010) who suggested that FUV can be the main regulator of star formation in the ISM.

For cases that have both types of feedback, the fit to NGC 5055 is quite close. In particular, we are encouraged by the fact that the KS relation is much tighter for this individual galaxy than the large spread in the entire population as is to be expected for any individual galaxy.

On closer inspection there is an offset at higher surface densities such that the slope is somewhat steeper. Given the large variation in slopes for individual galaxies with the overall distribution (e.g. Ostriker et al. 2010), this is not a concern. It is possible to fit slopes to the individual galaxy KS relation above $\Sigma_g > 10\,\mathrm{M_\odot\,pc^{-2}}$. These slopes are 2.39, 2.36, 2.12, 2.14, and -2.27 for cases FUVFB50, FUVFB10, FB50, FB10, and FUV*, respectively. Kennicutt (1998) notes that slopes from 1.29 up to 2.47 can be fit to an overall sample of galaxies in this range depending on the fitting approach employed. This calls into question the value of fitting slopes in a limited region near $10\,\mathrm{M_\odot\,pc^{-2}}$.

We do note that cases with higher feedback provide a modestly better fit but this is not particularly significant. In particular, our chosen range of SN energies is acceptable but the fit favours higher energies in this instance. Further, our simulations do not include the full range of early stellar feedback physics. It is possible that stellar winds, radiation pressure or photoionization play a role in setting the KS slope in high surface density regime, which could also account for the steeper slopes observed.

We wish to be clear regarding the interpretation of our plotted KS relation. First, the goal is not to match the general relation for galaxy samples, such as that of Kennicutt (1998), with its commonly cited power law of $\Sigma^{1.4}$. In the relevant region, near $10\,\mathrm{M_\odot\,pc^{-2}}$ in the left-hand panels of Fig. 5, the general relation not only steepens but the spread becomes so large that merely being inside the range of the data is fairly meaningless. Rather, we are comparing our specific galaxy to the individual relation for NGC 5055 which has similar radial profiles. In this case, we see quite similar curves (as shown in the right-hand panels of the figure) except for the FUV-only case. A key point is how tight the relation is for a specific galaxy.

Compared to NGC 5055, the simulations have a similarly tight relation with a moderately steeper slope. As outlined in Paper I, high stellar densities imply a higher total pressure and more star formation. This connection has been demonstrated observationally by Gallagher et al. (2018), among others. Referring back to Fig. 1, NGC 5055 has a systematically higher stellar surface density, Σ_*, at each radius but accurate scale heights are needed to convert that to a density. We note that the similarity to NGC 5055 is somewhat coincidental. The AGORA galaxy was not intended to fit NGC 5055. Several key properties (e.g. the rotation curve, giving the dark matter vertical gravity, and the stellar scale heights) were not matched. Increasing the stellar scale height can dramatically reduce the gravity due to stars and lower the pressure and SFRs. Thus, a galaxy model that better approximates NGC 5055 would be required before we could investigate the offset and slope in more detail. Matching the high surface density, innermost regions well might also require a model for molecular hydrogen which is expected to dominate there.

If we look to lower surface densities, $\Sigma_g \lesssim 3\,\mathrm{M_\odot\,pc^{-2}}$, the SFRs appear consistent in all cases, including FUV$\star$. We expect FUV heating to be most important in the outer regions of disc galaxies. Based on these first results, it appears that simulated galaxies require SNe feedback for the inner-mid disc and FUV heating may be sufficient for the outer disc.

Furthermore, FUV impacts the outer disc in a way that SN feedback cannot. As the FUV mean-free path is long, star formation
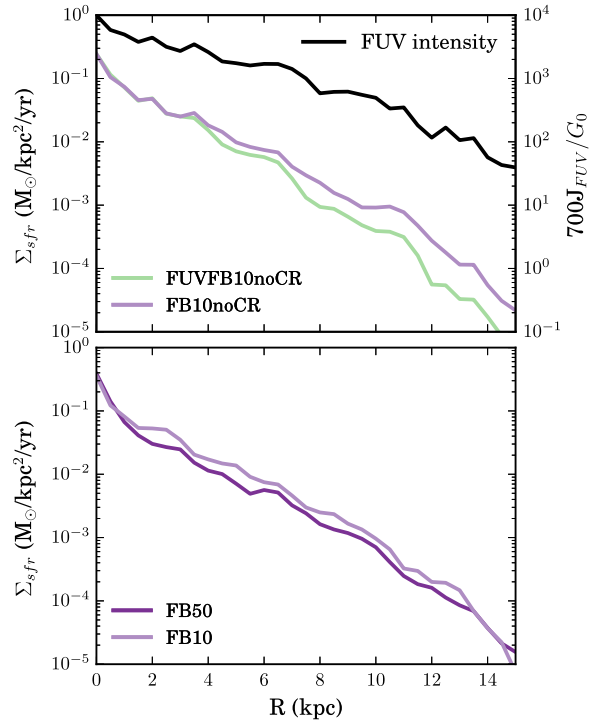

Figure 6. The SFR surface density as a function of radius for four galaxies in the suite. The inclusion of FUV radiation changes the slope of the SFR surface density relation, as shown in the top plot. In contrast, increasing the amount of energy from superbubble feedback changes the normalization of the SFR surface density curve but not the overall slope, as shown in the bottom plot. We posit that FUV radiation has the highest impact in the outer disc of galaxies. FUV radiation has a long mean-free path and thus can impact the ISM in a more long range way. This is shown by the FUV intensity, plotted as the black line in the top panel. This line does not share the same slope as the SFR surface density: if the feedback were localized they would share the same slope.

in the inner regions of the disc can heat the outer regions of the disc. This effect is shown in Fig. 6, where the purple and green lines denote the SFR surface density for galaxies with SNe feedback only and SNe with FUV feedback, respectively. In the outer disc, beyond ~6 kpc, there is a change in slope for the case with FUV added: star formation is suppressed to a larger degree. This is something that SNe alone cannot accomplish: increasing the SNe energy merely changes the normalization of this relation, not the slope (see the bottom panel of Fig. 6).

5 THE PHASES OF THE ISM

In Section 4.2, we saw that adding adding additional feedback on top of SNe feedback decreased their role in maintaining pressure support. We are also interested in how the inclusion of self-consistent FUV heating impacts the structure of the ISM. We begin by considering how gas is divided into the different temperature phases of the ISM. We make divisions for these phases as follows. Hot gas is any gas above 10^5 K and this gas has most likely been heated by superbubble feedback. Warm gas is any gas between 10^5 and 2000 K. Cold gas is any gas below 2000 K. FUV is the dominant heating mechanism for any gas that has not been heated by SNe. We add an additional category, cold gas which is eligible for star formation. This is any gas below 2000 K which has not been heated by superbubble feedback. This gas can form stars if its density exceeds 100 cm^{-3}.
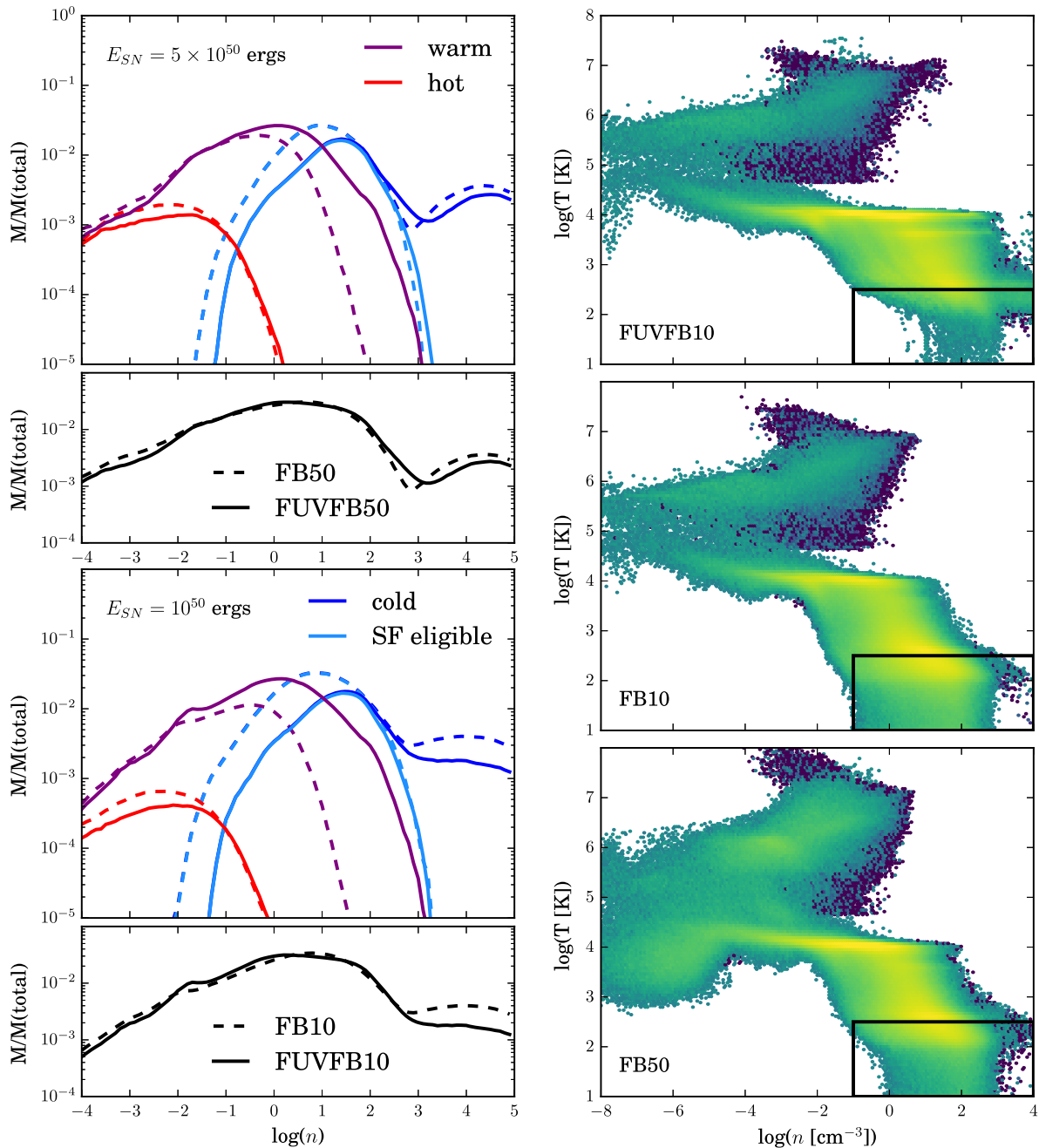
Figure 7. The density distribution for gas in different phases of the ISM. Hot gas (red) is any gas above 10^5 K and this gas has most likely been heated by superbubble feedback. Warm gas (purple) is any gas between 10^5 and 2000 K. Cold gas (blue) is any gas below 2000 K. Cold gas which is eligible for star formation (SF eligible, light blue) is any gas below 2000 K which has not been heated by superbubble feedback. The black lines show the distribution for all of the gas. Dashed lines denote cases that have only superbubble feedback, while solid lines have both superbubble and FUV heating. Shown another way, the phase diagrams for simulations FB10noCR and FUVFB10noCR. The phase diagrams are weighted by mass, with lighter colours denoting higher mass. The inclusion of FUV introduces more warm diffuse gas, which is more in line with what we expect in nature.

In the left-hand column of Fig. 7, the distribution of gas through different density bins is plotted for each of the temperature divisions outlined above. The top and bottom rows are separated by the strength of the superbubble feedback energy. The first noticeable difference is in the amount of warm gas: the inclusion of radiative transfer appreciably changes the distribution of warm neutral gas. The peak of the warm gas distribution remains near $n \sim 0.3\,\mathrm{cm}^{-3}$ in all cases. This matches expectations for the warm neutral phase of the ISM (Tielens

2005). However, when FUV heating is added on top of superbubble feedback there is more warm gas at higher densities, between 10 and $10^3\,\mathrm{cm}^{-3}$. This can be quantified by looking at the maximum density of the warm phase gas in each case. Considering the top two plots, adding FUV heating increases the maximum density of the warm phase gas by 1–2 orders of magnitude.

A complementary phenomenon is seen for the density distribution of cold gas. There is a decrease in the amount of both cold diffuse and

cold dense gas when the FUV heating is added (see cases FUVFB50 and FUVFB10). We note that a small fraction of the dense gas is not eligible for star formation because it is within two-phase particles. The portion of dense gas that is eligible for star formation is overplotted as the light blue line in Fig. 7. We make note of this mainly because using the superbubble model maintains a trace of high density gas, $\gtrsim 10^3$ cm^{-3}, that is absent otherwise.

These phase changes occur without significant changes to the total density distribution of the ISM. The black curves plotted in Fig. 7 show the total mass distribution at each density in the ISM for all of the temperature phases considered. The curves are very similar, with the only deviations being at the largest densities. This redistribution is particularly apparent when considering the warm medium. When FUV heating is included gas changes from being diffuse ($\lesssim 10$ cm^{-3}) and cold, to being diffuse and warm. However, the density structure at those densities remains mostly unchanged, only the temperature distribution is impacted. This can be seen very clearly in Fig. 7.

Another way to conceptualize this is by using the phase diagram, which plots the 2D distribution of mass in the density–temperature space. In the right-hand column of Fig. 7, we plot the phase diagrams for three of the galaxies. If we contrast the top two plots, showing the phase diagrams for FUVFB10 and FB10, we can see that the greatest differences occur at low temperatures. The black box is drawn to aid the eye in comparing the diagrams. The case with FUV radiation has significantly less gas at low densities (< 10 cm^{-3}) and low temperatures (< 500 K). Gas at these low densities should not populate the cold neutral medium, it too diffuse. The inclusion of the radiation allows it to be replaced by warm neutral counterparts. This is something that SN feedback alone cannot do. In the bottom plot, the result for FB50 is shown. This has five times more SN energy than the case above (FB10) and a similar phase diagram.

This outcome can be understood through pressure requirements. In the top left and top middle panels of Fig. 4, a comparison of the relative amount of the total pressure in a P_{hot}, SNe heated component, and P_{th}, warm thermal component are shown. When FUV radiation is included a larger amount of the total pressure support comes from the thermal component, decreasing the amount of support that needs to come from an SNe heated component. In the phase diagram, this translates to a larger amount of warm gas. When we do not use the FUV radiation, in general the ISM is quite cold across a large range of densities and SNe are only capable of making this gas hot or stirring it up. FUV provides us with an intermediate step, where we can have a high pressure warm medium, as seen in Fig. 4. This shows a crucial role for FUV radiation in maintaining a phase of warm neutral gas.

6 SUMMARY AND CONCLUSIONS

For the first time, we have simulated a full, isolated galaxy using a self-consistent treatment for FUV photoelectric heating via dust grains of the typical ISM, implemented through a ray-tracing approach to radiative transfer with absorption. We used a relatively low dust opacity of 300 cm^2 g^{-1} (scaled linearly from solar metallicity) as in Wolfire et al. (2003) and a fixed heating efficiency of 3 per cent. This can be taken as an upper bound on the effectiveness of this heating for the typical ISM. We do not model molecular hydrogen and thus the dissociating effects of FUV are not included. We have explored the effect of FUV alone and in combination with a highly constrained model for SN feedback.

The KS relation for individual galaxies is quite tight compared to the overall relation covering the full population, which has spread of 1–2 dex. The AGORA isolated galaxy we simulate here is fortuitously similar to NGC 5055. We get a similarly tight KS relation from

simulations using both FUV and SNe together, including its small spread of < 0.5 dex. A small spread and significant slope variations are strongly indicated for individual galaxies (Ostriker et al. 2010) and thus should be expected in simulations. This result strongly supports the importance of secondary parameters, such as the stellar density, in setting the SFR, as championed by Blitz & Rosolowsky (2006). This shows that our full model is both physical and consistent with established relations. The only free parameter is the energy per SN and a factor of 5 variation still results in simulations that are reasonable fits. The KS relation fit marginally favours higher net SNe energy (50 per cent internal losses or $\sim 5 \times 10^{50}$ erg per SN) and there are indications of a small slope difference. These differences are far smaller than the spread in the full KS galaxies data set. Better galaxy models will be required to confirm these differences given that the AGORA galaxy model was not built to match NGC 5055 specifically.

We find that FUV heating on its own is not sufficient to regulate star formation. In this case, the galaxy rapidly consumes the available fuel. This is in contrast to the Ostriker et al. (2010) framework, which linked regulation to FUV heating. The mode of failure of FUV regulation is important for future analytical attempts to model galactic star formation regulation. Simulations with ineffective feedback result in a very clumpy ISM and this behaviour is qualitatively the same as no feedback at all. The driver of clump formation is converging flows in the $r - \phi$ plane which are implicitly excluded by assumed smooth radial density profiles in analytical models. The moderate temperatures generated by FUV cannot unbind these large clumps and they dominate the evolution going forward, sweeping up most of the gas mass. This behaviour was also seen in the AGORA isolated simulations of this galaxy (Kim et al. 2016). These used either no feedback or purely thermal SN feedback, which is well known to be ineffective (Katz 1992). The key difference from this work is that in AGORA, the star formation efficiency was very low (about 1 per cent per free-fall time) and a stiff equation of state prevented dense gas with short free-fall times. This brought the total SFRs closer to Milky Way-like expectations. However, most of the mass is still in massive clumps exceeding 500 M$_\odot$ pc^{-2}, which in turn produce large star clusters.

In combination with the SN feedback, we see that the addition of FUV radiation has important impacts on the ISM. Our results confirm that FUV heating is non-local and that the gas state depends on distant sources ($\gtrsim 6$ kpc) and correct absorption by the intervening material. The inclusion of FUV heating helps regulate star formation in a more gentle way. FUV heating is able to produce regulated galaxies with realistic scale heights. We can see this when looking at the distribution of gas among the hot, warm, and cold phases of the ISM. FUV heating is able to move substantial mass from the cold gas into the warm neutral phase. This provides significant pressure so that less star formation is needed, particularly in the outer disc. Our analysis confirms that the required pressure (as employed in Paper I) provides a robust framework to understand how different feedback mechanisms combine to regulate star formation and structure in the ISM of galaxies.

A potential focus for future work is the outer disc where FUV provides a large portion of the support. In our results, the drop off in star formation is significantly different for SNe feedback runs with and without self-consistent FUV (Fig. 6). These differences may depend on how star formation is modelled. In future work, we will explore more complex star formation models more closely tied to the cold, dense phase (e.g. Semenov et al. 2018). Observationally, this low surface density regime is difficult to measure accurately but it could provide important insights into how star formation and ISM structure are linked to FUV, turbulence, and other feedback.

This work indicates that fitting star formation expectations while producing a realistic ISM can provide powerful constraints on how different feedback processes function in real galaxies. As in Paper I (Benincasa et al. 2016), we find that no one star formation or ISM diagnostic on its own can tell the whole story. The KS relation (Fig. 5) provides an illustration of this point. If we study the right-hand panels of this figure, which feature direct comparisons to NGC 5055, all of the galaxies that were able to regulate their star formation provide a convincing match. We know from our other diagnostics that they have significantly different overall SFRs, different scale heights, and different ISMs. Thus, we should perform careful comparisons to observed galaxies involving all of these properties and not just SFRs. In particular, the low SN energy plus FUV case provides the best match to the scale height observations of Patra (2019) for NGC 5055 (Fig. 3). Our galaxy is a passable proxy for NGC 5055 but there are differences in the profiles of both gas and stars, as well as the rotation curve. In order to make these comparison properly, we should use galaxies that are designed specifically to match observed galaxies. This will be a target of future work.

ACKNOWLEDGEMENTS

DATA AVAILABILITY

The data underlying this article will be shared on reasonable request to the corresponding author.

REFERENCES

Agertz O., Romeo A. B., Grisdale K., 2015, MNRAS, 449, 2156
Aubert D., Teyssier R., 2008, MNRAS, 387, 295
Benincasa S. M., Tasker E. J., Pudritz R. E., Wadsley J., 2013, ApJ, 776, 23
Benincasa S. M., Wadsley J., Couchman H. M. P., Keller B. W., 2016, MNRAS, 462, 3053
Bigiel F., Leroy A., Walter F., Brinks E., de Blok W. J. G., Madore B., Thornley M. D., 2008, AJ, 136, 2846
Blitz L., Rosolowsky E., 2004, ApJ, 612, L29
Blitz L., Rosolowsky E., 2006, ApJ, 650, 933
Brinchmann J., Charlot S., White S. D. M., Tremonti C., Kauffmann G., Heckman T., Brinkmann J., 2004, MNRAS, 351, 1151
Byun Y. I., Freeman K. C., Kylafis N. D., 1994, ApJ, 432, 114
Daddi E. et al., 2007, ApJ, 670, 156

Davis S. W., Jiang Y.-F., Stone J. M., Murray N., 2014, ApJ, 796, 107
Diemer B. et al., 2018, ApJS, 238, 33
Dobbs C. L., Pettitt A. R., Corbelli E., Pringle J. E., 2018, MNRAS, 478, 3793
Draine B. T., 1978, ApJS, 36, 595
Duarte-Cabral A., Dobbs C. L., 2017, MNRAS, 470, 4261
El-Badry K., Ostriker E. C., Kim C.-G., Quataert E., Weisz D. R., 2019, MNRAS, 478, 3793
Elmegreen B. G., Parravano A., 1994, ApJ, 435, L121
Forbes J. C., Krumholz M. R., Goldbaum N. J., Dekel A., 2016, Nature, 535, 523
Gallagher M. J. et al., 2018, ApJ, 858, 90
Gentry E. S., Madau P., Krumholz M. R., 2020, MNRAS, 492, 1243
Gnedin N. Y., Tassis K., Kravtsov A. V., 2009, ApJ, 697, 55
Grisdale K., Agertz O., Romeo A. B., Renaud F., Read J. I., 2017, MNRAS, 466, 1093
Grisdale K., Agertz O., Renaud F., Romeo A. B., 2018, MNRAS, 479, 3167
Grond J. J., Woods R. M., Wadsley J. W., Couchman H. M. P., 2019, MNRAS, 485, 3681
Hernquist L., 1990, ApJ, 356, 359
Herrera-Camus R. et al., 2017, ApJ, 835, 201
Hopkins P. F., Quataert E., Murray N., 2012, MNRAS, 421, 3488
Hopkins P. F., Grudić M. Y., Wetzel A., Kereš D., Faucher-Giguère C.-A., Ma X., Murray N., Butcher N., 2020, MNRAS, 491, 3702
Hsieh B. C. et al., 2017, ApJ, 851, L24
Hu C.-Y., Naab T., Glover S. C. O., Walch S., Clark P. C., 2017, MNRAS, 471, 2151
Kannan R., Vogelsberger M., Marinacci F., McKinnon R., Pakmor R., Springel V., 2019, MNRAS, 485, 117
Katz N., 1992, ApJ, 391, 502
Keller B. W., Wadsley J., Benincasa S. M., Couchman H. M. P., 2014, MNRAS, 442, 3013
Keller B. W., Wadsley J., Couchman H. M. P., 2015, MNRAS, 453, 3499
Keller B. W., Wadsley J., Couchman H. M. P., 2016, MNRAS, 463, 1431
Kennicutt R. C., Jr, et al., 2007, ApJ, 671, 333
Kennicutt R. C., Jr., 1998, ApJ, 498, 541
Kennicutt R. C., Evans N. J., 2012, ARA&A, 50, 531
Kim J.-h. et al., 2014, ApJS, 210, 14
Kim J.-h. et al., 2016, ApJ, 833, 202
Kim C.-G., Ostriker E. C., 2015, ApJ, 815, 67
Kim C.-G., Kim W.-T., Ostriker E. C., 2011, ApJ, 743, 25
Krumholz M. R., Dekel A., McKee C. F., 2012, ApJ, 745, 69
Lagos C. d. P. et al., 2015, MNRAS, 452, 3815
Leitherer C. et al., 1999, ApJS, 123, 3
Leroy A. K., Walter F., Brinks E., Bigiel F., de Blok W. J. G., Madore B., Thornley M. D., 2008, AJ, 136, 2782
Leroy A. K. et al., 2009, AJ, 137, 4670
Marinacci F., Grand R. J. J., Pakmor R., Springel V., Gómez F. A., Frenk C. S., White S. D. M., 2017, MNRAS, 466, 3859
Murphy E. J. et al., 2011, ApJ, 737, 67
Nakanishi H., Sofue Y., 2016, PASJ, 68, 5
Navarro J. F., Frenk C. S., White S. D. M., 1997, ApJ, 490, 493
Nguyen N. K., Pettitt A. R., Tasker E. J., Okamoto T., 2018, MNRAS, 475, 27
Noeske K. G. et al., 2007, ApJ, 660, L43
Oñorbe J., Boylan-Kolchin M., Bullock J. S., Hopkins P. F., Kereš D., Faucher-Giguère C.-A., Quataert E., Murray N., 2015, MNRAS, 454, 2092
Ostriker E. C., Shetty R., 2011, ApJ, 731, 41
Ostriker E. C., McKee C. F., Leroy A. K., 2010, ApJ, 721, 975
Pan H.-A., Fujimoto Y., Tasker E. J., Rosolowsky E., Colombo D., Benincasa S. M., Wadsley J., 2015, MNRAS, 453, 3082
Patra N. N., 2019, MNRAS, 484, 81
Pettitt A. R., Egusa F., Dobbs C. L., Tasker E. J., Fujimoto Y., Habe A., 2018, MNRAS, 480, 3356
Rey-Raposo R., Dobbs C., Agertz O., Alig C., 2017, MNRAS, 464, 3536
Rosdahl J., Blaizot J., Aubert D., Stranex T., Teyssier R., 2013, MNRAS, 436, 2188
Rosdahl J., Schaye J., Teyssier R., Agertz O., 2015, MNRAS, 451, 34

Saintonge A. et al., 2017, ApJS, 233, 22
Salim S. et al., 2007, ApJS, 173, 267
Schaye J., 2004, ApJ, 609, 667
Schmidt M., 1959, ApJ, 129, 243
Semenov V. A., Kravtsov A. V., Gnedin N. Y., 2017, ApJ, 845, 133
Semenov V. A., Kravtsov A. V., Gnedin N. Y., 2018, ApJ, 861, 4
Shetty R., Ostriker E. C., 2012, ApJ, 754, 2
Shi Y. et al., 2018, ApJ, 853, 149
Springel V., Hernquist L., 2003, MNRAS, 339, 289
Tasker E. J., Tan J. C., 2009, ApJ, 700, 358
Tielens A. G. G. M., 2005, The Physics and Chemistry of the Interstellar Medium. Cambridge University Press, Cambridge, UK
Wadsley J. W., Stadel J., Quinn T., 2004, New Astron., 9, 137
Wadsley J. W., Keller B. W., Quinn T. R., 2017, MNRAS, 471, 2357
Walter F., Brinks E., de Blok W. J. G., Bigiel F., Kennicutt R. C., Jr., Thornley M. D., Leroy A., 2008, AJ, 136, 2563
Wang W. et al., 2018, ApJ, 869, 161
Watson W. D., 1972, ApJ, 176, 103
Weaver R., McCray R., Castor J., Shapiro P., Moore R., 1977, ApJ, 218, 377
Wolfire M. G., Hollenbach D., McKee C. F., Tielens A. G. G. M., Bakes E. L. O., 1995, ApJ, 443, 152
Wolfire M. G., McKee C. F., Hollenbach D., Tielens A. G. G. M., 2003, ApJ, 587, 278
Wong T., Blitz L., 2002, ApJ, 569, 157
Woods R., 2015, PhD thesis, McMaster University

APPENDIX A: RADIATIVE TRANSFER COMPARISONS

This work employed the original version of TREVR (Woods 2015). The most recent version, as discussed in Grond et al. (2019), has a modified ray trace and adaptive ray refinement to control errors. It does this by estimating the maximum optical depth error for each ray segment. If this exceeds the τ_{REFINE} parameter, the ray is split and re-tested until it succeeds or reaches the resolution limit. Grond et al. (2019) showed that this typically limits the overall optical depth errors to $\tau_{\mathrm{REFINE}}/10$ (with similar flux errors if $\tau_{\mathrm{REFINE}} \lesssim 1$). Thus, for $\tau_{\mathrm{REFINE}} = 0.01$, the results are equivalent to full-resolution ray traces which provides an accurate answer for comparisons. Conversely, $\tau_{\mathrm{REFINE}} = \infty$ means no added refinement for the new code and results in similar levels of error (but not the same results) as the original code. The new code is considerably slower (by more than an order of magnitude) than the original version used here and thus impractical to use for full runs. However, we applied it on a single evolved output at 400 Myr (FUVFB10) where SFRs and the ISM properties have reached a statistical steady state, allowing us to estimate the accuracy of the radiative transfer used for the current work.
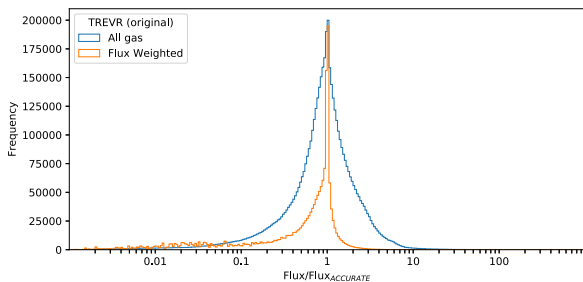

Figure A1. Flux errors for original TREVR (used in the current work) compared against an extremely accurate flux estimate using the most recent version ($\tau_{\mathrm{REFINE}} = 0.01$). This all gas curve is mass weighted and includes regions receiving low or negligible flux. The flux-weighted distribution shows errors weighted by the total flux received.
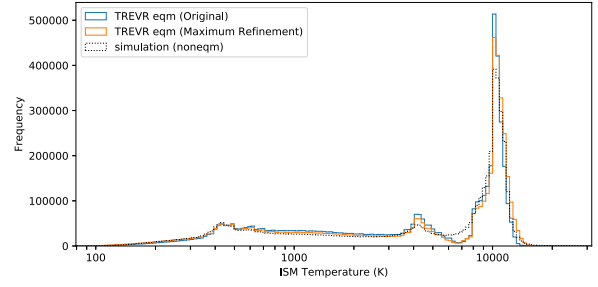

Figure A2. Equilibrium temperature distribution (including just the dominant photoelectric heating and radiative cooling) for original TREVR (used in the current work) compared to an extremely accurate flux estimate using the most recent version ($\tau_{\mathrm{REFINE}} = 0.01$). The dotted curve is the non-equilibrium temperature distribution in the full simulation output that was used.
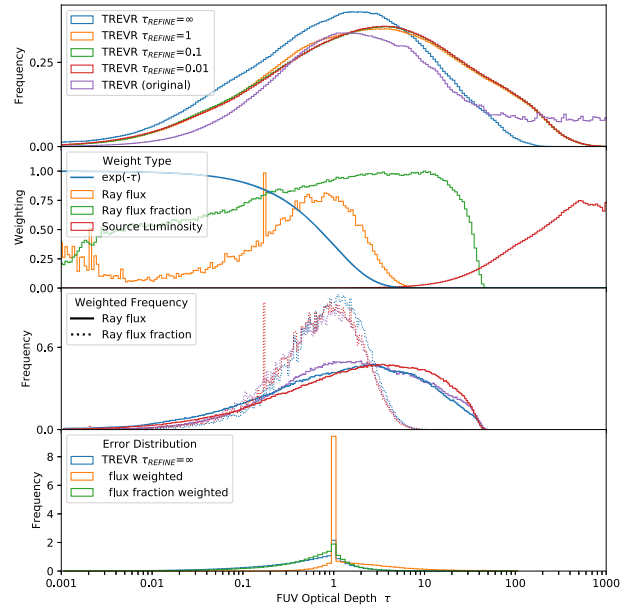

Figure A3. Detailed ray-by-ray comparison of the original TREVR to the most recent version with different refinement criteria. The original TREVR had no refinement error control, as does the newest version when $\tau_{\mathrm{REFINE}} = \infty$. The new version becomes extremely accurate for $\tau_{\mathrm{REFINE}} \lesssim 0.1$. The top panel shows the frequency of FUV optical depths per ray. The second panel shows various ways to weight the importance of they rays: attenuation ($e^{-\tau}$), received flux by the gas from the ray, received flux as a fraction of the total received by that particle and source luminosity. This confirms that most luminous sources are blocked by high columns and contribute little. The third panel shows the optical depth weighted for each ray's flux and flux fraction. The bottom panel shows the per ray optical depths for the least accurate TREVR relative to the most accurate TREVR refinement tested ($\tau_{\mathrm{REFINE}} = 0.01$).

Fig. A1 shows the flux errors for the representative output using the original scheme relative to an extremely accurate estimate (TREVR with $\tau_{\mathrm{REFINE}} = 0.01$). The wider distribution is for all gas, including gas with relatively little flux (i.e. where FUV is a minor contributor to the heating). The narrow distribution is flux weighted and demonstrates TREVR's small, absolute flux errors. The majority of the gas is within a few per cent of the accurate prediction. This avoids significant differences in the FUV heating. We characterize this via a temperature histogram for the ISM, shown in Fig. A2. As we were unable to perform a full run with the extremely accurate version, we computed equilibrium temperatures with just

photoelectric heating and radiative cooling for both the original code and accurate error controls on a single output. We focus on ISM conditions, where FUV is the dominant heating. The distributions are nearly identical. For comparison, we include the non-equilibrium distribution from the raw simulation output (dotted), which is almost the same. This demonstrates the dominance of FUV heating in this regime.

Radiative transfer with absorption is very challenging numerically, especially when a single resolution element can be optically thick, such as for UV in galaxies. Small offsets can dramatically change received fluxes. Following the appendix in Hopkins et al. (2012), we examined the optical depth distribution between sources and gas and show the results in Fig. A3. We focus on the importance of examining the optical depth errors for radiation bands of interest, rather than the full column density distribution. For FUV, columns less than 10^{21} cm^{-2} are most important, as this is where the optical depth is $\lesssim 30$ (this may be compared to fig. A1 in Hopkins et al. 2012 for the local absorption estimator, LEBRON).

The top panel of Fig. A3 shows the raw distribution of optical depths for TREVR on the representative output with different accuracy criteria applied. One particle in 100 was used and each receives input from ~ 1400 rays. The differences are largest for extreme optical depths ($\gtrsim 30$). To extract useful information from this distribution we must weight the rays based on their effect. The second panel shows potential weights: attenuation ($e^{-\tau}$), flux at the receiving gas and the relative flux contribution (out of all rays hitting the specific gas particle). The second weighting emphasizes rays that deliver high fluxes. The third weighting selects rays that are most important for a specific gas element (i.e. influencing its heating and temperature). We also show luminosity weighting. This last is less useful as it favours rays from sources that are highly obscured and contribute little to the radiation field for the vast majority of the gas. When we convolve the distributions with weights that reflect the impact on the gas, we see that the original TREVR is fairly similar to the new version. The bottom panel shows a distribution of optical depth ratios, where 1 indicates a match to the most accurate TREVR run. These distributions, tightly clustered around the correct optical depth, enable the good overall flux error distribution shown in Fig. A1.

Naturally, the most intensely irradiated gas is within a few pc of bright, young sources. However, these sources tend to be deeply embedded. The vast majority of the ISM experiences moderate fluxes. The third panel of Fig. A3 shows that rays with optical depths between 0.1 and 10 are most important in determining the flux in the typical ISM, corresponding to sources that are either more evolved and/or have more favourable sightlines. Half the flux for a typical parcel of gas is from distances of 6.4 kpc or more. These factors confirm the importance of absorbing material in the several kpc between the gas and its influential sources.

This paper has been typeset from a TeX/LaTeX file prepared by the author.